JGR Space Physics

RESEARCH ARTICLE
10.1029/2020JA028283

Excitation Mechanism of Ionospheric 6-Day Oscillation During the 2019 September Sudden Stratospheric Warming Event

Yasunobu Miyoshi[1] and **Yosuke Yamazaki**[2]

[1]Department of Earth and Planetary Sciences, Kyushu University, Fukuoka, Japan, [2]GFZ German Research Center for Geosciences, Potsdam, Germany

Key Points:
- We examine ionospheric 6-day oscillation during the September 2019 SSW event using GAIA simulations
- The 6-day oscillation is generated not by the 6-day wave but by 10–14 hr waves
- The nonlinear interaction between the 6-day wave and tides leads to a 6-day modulation of the 10–14 hr waves

Supporting Information:
- Supporting information S1
- Figure S1
- Figure S2
- Figure S3
- Figure S4
- Table S1

Correspondence to:
Y. Miyoshi,
y.miyoshi.527@m.kyushu-u.ac.jp

Citation:
Miyoshi, Y., & Yamazaki, Y. (2020). Excitation mechanism of ionospheric 6-day oscillation during the 2019 September sudden stratospheric warming event. *Journal of Geophysical Research: Space Physics*, *125*, e2020JA028283. https://doi.org/10.1029/2020JA028283

Received 29 MAY 2020
Accepted 11 JUL 2020
Accepted article online 21 AUG 2020

Abstract A sudden stratospheric warming (SSW) event in the Antarctic region occurred in September 2019. During the SSW event, the quasi 6-day wave (Q6DW) was enhanced in the mesosphere, and strong 6-day oscillations are observed in ionospheric parameters, such as the equatorial electrojet (EEJ) and electron density. The 6-day variation in the EEJ has a westward moving structure with the zonal wave number 1, indicating the influence of the Q6DW. In this study, we investigate the excitation mechanism of the 6-day variations in the EEJ and electron density using numerical simulations. The main results are as follows. The 6-day variations in the ionosphere are not generated by the Q6DW but generated by the waves with periods from 10 to 14 hr. The amplitude of the 10–14 hr waves is modulated with a period of 6 days, due to the nonlinear interaction between the Q6DW and migrating semidiurnal tide. This leads to the 6-day variations in the EEJ and electron density through the *E* region dynamo process. At a fixed local time, the secondary waves generated by the Q6DW-tidal interaction produce westward moving ionospheric 6-day variations with zonal wave number 1, which cannot be distinguished from the ionospheric variations by the Q6DW itself. The interference of secondary waves leads to a longitudinal asymmetry in the magnitude of the ionospheric 6-day oscillation.

1. Introduction

A 5–6 day oscillation is one of the significant variations in the mesosphere and lower thermosphere (MLT) region. A 5–6 day oscillation is considered to be caused by the Rossby wave having zonal wave number 1 ($s = 1$), which is widely recognized as the first symmetric normal mode Rossby wave derived from the classical tidal theory (Hirota & Hirooka, 1984; Madden & Julian, 1972). The dominant period of the first symmetric normal mode with $s = 1$ is about 5 days under the isothermal/motionless condition, so this wave is called "5-day wave" (Salby, 1981). However, satellite observations (Riggin et al., 2006; Wu et al., 1994) indicated that the dominant period in the MLT shifted to about 6 days. Thus, the first symmetric normal mode is often called "quasi-6-day wave (Q6DW)." Using SABER temperature measurements, Pancheva et al. (2010) showed that the Q6DW is more active during equinoxes and the Q6DW amplitude reaches the maximum at 105–110 km height.

Observational studies have revealed a 6-day oscillation in the ionosphere. Takahashi et al. (2006) reported a 6–8 day oscillation of the *F* layer height near the equator. Liu et al. (2010) showed that the wave 4 longitudinal structure of the *F* layer height fluctuates with a period of 6 days. Gu et al. (2014) and Yamazaki (2018) observed the 6-day oscillation of the total electron content (TEC). Moreover, using CHAMP, Swarm, and Aura satellites, Yamazaki et al. (2018) showed that the 6-day variation in the equatorial electrojet (EEJ) intensity occurs when the amplitude of the Q6DW in the mesosphere is enhanced. The 6-day variation in the EEJ has a westward moving $s = 1$ structure, indicating the influence of the Q6DW. Yamazaki et al. (2018) also pointed out that the amplitude of the 6-day variation in the EEJ has a strong longitudinal dependence although the Q6DW is a global-scale wave with $s = 1$. For example, the amplitude of the 6-day variation during the September 2006 event is enhanced at 180–210°E whereas the 6-day variation of the May 2007 event is most pronounced at 140–170°E. Thus, there is no systematic longitudinal dependence. The reason for this longitudinal dependence still remains unclear.

Whole atmosphere–ionosphere coupled models are powerful tools to investigate the effects of the atmospheric waves from the lower atmosphere on the ionosphere through the coupling processes between the

neutrals and plasmas (Fuller-Rowel et al., 2010; Jin et al., 2011; Liu et al., 2010). Using TIME-GCM, Gan et al. (2016, 2017) investigated impacts of the Q6DW on the ionosphere, imposing the wind variation due to the Q6DW in the lower boundary (30 km height). The 6-day variation in the ionosphere is explained by the 6-day variation in the daytime E region electric field generated by the neutral wind variation. They showed that the secondary waves that are generated by the nonlinear interaction between the Q6DW and migrating diurnal/semidiurnal tides play an important role on the 6-day variation in the ionosphere. Using the SABER temperature measurements, Forbes and Zhang (2017) found signatures of the secondary waves due to the Q6DW-tide nonlinear interaction in the MLT. For example, the nonlinear interaction between the Q6DW and migrating diurnal tide generates westward moving $s = 2$ component with a period of 21 hr and $s = 0$ component with a period of 29 hr. However, it is not clear how these secondary waves contribute to the 6-day variation in the ionosphere and how the secondary waves affect the longitudinal structure of the 6-day variation in the ionosphere.

Yamazaki et al. (2020; hereafter Y20) reported the sudden stratospheric warming (SSW) event occurred in the Southern Hemisphere (SH) in September 2019 and its impact on the ionosphere. The temperature at 30 km height in the Antarctica increased by 50 K within a week, and the stratomesospheric jet in the SH was attenuated. Interestingly, the Q6DW activity in the mesosphere was also enhanced. Swarm satellite observations revealed that the 6-day variation in the EEJ and electron density is prominent during the SSW event. The variation in the EEJ shows a westward moving $s = 1$ structure, indicating the influence of the Q6DW. However, due to insufficient neutral wind observations in the lower thermosphere, the interaction processes between plasma and neutrals through the E region dynamo are not well understood. Namely, it is not clear how the 6-day variations in the ionosphere are connected with the Q6DW in the MLT. Therefore, using a whole atmosphere–ionosphere coupled model, the excitation mechanism of the 6-day variation in the EEJ is examined in this study. In particular, we focus on the behavior of the secondary waves generated by the Q6DW-tide nonlinear interaction and its influence on the 6-day variation in the ionosphere. This paper is organized as follows. The model and numerical simulation are briefly described in section 2. The results and discussion are given sections 3 and 4, respectively. Finally, our concluding remarks are presented in section 5.

2. Description of the Model and Numerical Simulation

The Ground-to-topside model of Atmosphere and Ionosphere for Aeronomy (GAIA) is a whole atmosphere–ionosphere coupled model that covers atmospheric regions from the ground surface to the exobase without any artificial boundaries between the lower and upper regions. GAIA has been developed by integrating three models: a general circulation model (GCM) of the neutral atmosphere, an ionosphere model, and an electrodynamics model. It is noteworthy that GAIA incorporates the interaction processes between plasma and neutral species. A detailed description of GAIA can be found in Jin et al. (2011) and Miyoshi et al. (2012, 2017).

For the neutral atmospheric part, a whole atmosphere GCM from the ground surface to the exobase (Miyoshi & Fujiwara, 2003, 2006) is used. The GCM used here is a global spectral model with a maximum horizontal wave number of 42 and has 150 vertical layers with a vertical resolution of 0.2 scale heights. The GCM includes a full set of physical processes appropriate for the whole atmospheric region. For example, moist convection scheme, a hydrological cycle, boundary layer process, and radiation process are included in the troposphere. The effects of topography are also taken into account. In the thermosphere, the model estimates the interaction processes between neutrals and plasmas, such as ion drag, Joule heating, and auroral precipitation heating. Meteorological reanalysis data provided by the Japan Meteorological Agency (JRA55) (Kobayashi et al., 2015) are incorporated below a height of 40 km by a nudging method. The nudging method forces physical variables, such as the surface pressure, temperature, zonal and meridional winds, and water vapor, to the JRA55 data. This means that the GCM can reproduce realistic temporal and spatial variations in the general circulation in the troposphere and lower stratosphere.

For the ionospheric part, the dynamics and chemical processes of the major ion species (O^+, $O_2{}^+$, $N_2{}^+$, and NO^+) are taken into account (Shinagawa, 2009). The horizontal resolution is 2.5° longitude by 1.0° latitude. The ionosphere model extends from the ground surface to about 2,000 km height. The coupling processes between plasma and neutral species are also incorporated. The electrodynamics model (Jin et al., 2008)

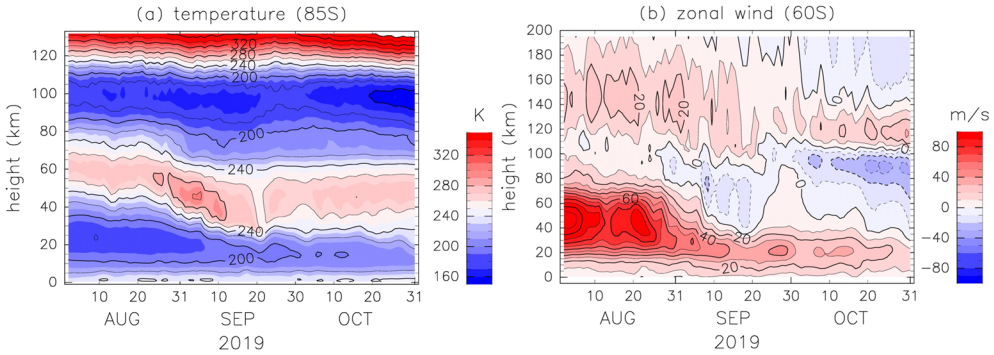

Figure 1. (a) Height-time distribution of the zonal mean temperature at 85°S. Units are K. (b) As in Figure 1a but for the zonal mean zonal wind at 60°S. Positive and negative values indicate eastward and westward winds, respectively. Units are m/s.

calculates the global distribution of the ionospheric currents and electric fields at every 5 min. The model uses a tilted dipole geomagnetic field and assumes equipotential magnetic field lines.

The numerical simulation was performed under solar minimum and geomagnetically quiet conditions to exclude influences from temporal variations in the solar UV/EUV fluxes and geomagnetic activity. The solar $F10.7$ flux was set to 68×10^{-22} W m^{-2} Hz^{-1}, which is the monthly mean value in September 2019, and the cross polar potential was fixed at 30 kV. We performed numerical simulation for 2019. The simulation data were output at 30 min intervals. In the present study, we analyze the data for the period from 1 August to 31 October 2019. The simulation data are archived at GFZ Data Services (Yamazaki & Miyoshi, 2020).

3. Results

3.1. SSW and Q6DW in September 2019

Y20 reported that an SSW event occurred in the Antarctic region in September 2019 and that the Q6DW in the stratosphere and mesosphere were enhanced after the SSW. We first examine how well GAIA can reproduce the SSW event in September 2019. Figure 1a shows the height-time distribution of the zonal mean temperature near the South Pole (85°S) simulated by GAIA. The temperature in the stratosphere increases during the period from 20 August to 15 September. The temperature rise within a week in early September is about 50 K at 30 km. The stratomesospheric eastward jet is attenuated after 20 August, and the westward wind appears in the 80–110 km height region on 25 August (Figure 1b). The westward wind region extends downward and reaches at 36 km height on 18 September. However, this event is a minor SSW because the reversal of the zonal wind direction did not occur at 30 km height. The simulated features of the SSW event agree well with those observed by the Microwave Limb Sounder (MLS) on the Aura satellite and the MERRA-2 reanalysis data (Gelaro et al., 2017) (Y20).

The behavior of the Q6DW simulated by the GAIA is examined next. The procedure to detect the Q6DW is as follows. Using a space-time spectral analysis (Hayashi, 1971), westward moving component of $s = 1$ is extracted. Next a band-pass filter is applied to separate the dominant periods for the Q6DW (5.0 to 7.0 days). The method to extract the Q6DW is the same with that used in Miyoshi and Hirooka (1999, 2003) and Miyoshi (1999). Figure 2a shows the temporal variation in the geopotential component of the Q6DW at 95 km height, where the Q6DW amplitude reaches its maximum. The Q6DW was enhanced during 13 September to 3 October, with the maximum of 0.45 km occurring on 23–25 September. Another weak Q6DW event occurred on 25 August to 3 September. Figure 2c shows the height-latitude distribution of the Q6DW amplitude (geopotential height component) averaged from 10 to 30 September. The amplitude below 95 km height has maxima at ±45° latitude and increases with increasing height. The maxima at 60 and 95 km are 0.15 and 0.35 km, respectively. The phase structure is symmetric about the equator (not shown). These features of the Q6DW is in good agreement with the observation (Figure 3 of Y20). This means that GAIA can reliably simulate the SSW and Q6DW events in September 2019. Note that the simulated latitudinal structure of the Q6DW is in agreement with that of the first symmetric mode of the normal mode Rossby wave derived by the classical tidal theory (Forbes & Zhang, 2017). The Q6DW amplitude in the

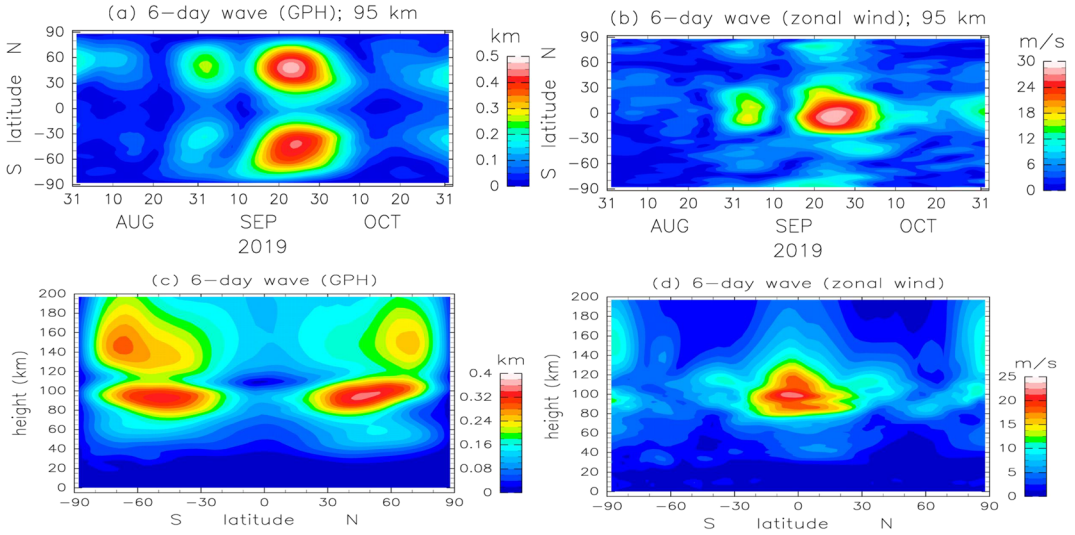

Figure 2. (a) Latitude–time distribution of the geopotential height component of the Q6DW amplitude at 95 km height. Units are km. (b) As in Figure 2a but for the zonal wind component. Units are m/s. (c) Height-latitude section of the Q6DW amplitude in geopotential height component averaged from 10 to 30 September 2019. Units are km. (d) As in Figure 2c but for the zonal wind component. Units are m/s.

100–120 km height region decreases with increasing height, whereas that in the 120–150 km height region increases with height. The attenuation of the Q6DW amplitude in the 100–120 km height is probably due to the large eddy vertical viscosity in the MLT. Above 120 km height, the peak of the Q6DW amplitude is located at ±65–70° latitude, and the latitudinal structure is different from that below 100 km height.

The zonal wind component of the Q6DW is largest at the equator, and secondary peaks are found at high latitudes (Figure 2b). The zonal wind component is enhanced during 13 September to 3 October, with the maximum value of 27 m/s at the equator. The height-latitude distribution of the zonal wind amplitude due to the Q6DW is shown in Figure 2d. The zonal wind amplitude reaches its maximum at 95 km and is less than 10 m/s above 150 km height. Note that the zonal wind amplitude in the 110–120 km height region, where the *E* region dynamo process is active, is about 20 m/s. As for the meridional wind component due to the Q6DW, the peak is located at ±45° latitude, and the peak values at heights of 60 and 95 km are 4 and 8 m/s, respectively (not shown).

3.2. EEJ Simulated by GAIA

Figure 3a shows the global distribution of the eastward electric current intensity (integrate from 80 to 150 km height) at 12 local time (LT) averaged in September 2019. A narrow band of strong eastward electric current is evident along the geomagnetic equator. This means that the GAIA can reproduce the EEJ. Figure 3b shows day-longitude distribution of the EEJ at 12LT. A wave 4 structure in the longitudinal direction is evident. The peaks of the EEJ intensity are located at around 0°E, 90°E, 180°E, and 90°W. The EEJ intensity is the largest at 80–110°E (90–130 mA/m) and the smallest at 100–130°W (50–90 mA/m). It is clearly seen that the EEJ oscillates with a period of 6 days. To see the 6 day oscillation in detail, Figure 3c shows the time-longitude distribution of the EEJ with a period from 5.0 to 7.0 days. A westward moving component of $s = 1$ with a period of 6 days is significant after 10 September. The amplitude of the 6 day oscillation ranges from 12 to 24 mA/m and maximizes at 60–120°W. These features of the simulated EEJ intensity also agree well with the Swarm observation (Y20).

Figure 4a shows the day-longitude distribution of the eastward electric field at 110 km height at 11–12 LT. The electric field values are averaged from 10°N to 10°S geomagnetic latitudes. The westward moving structure of $s = 1$ with a period of 6 days is clearly seen, and this feature is similar to that of the EEJ. This similarity is explained by the fact that the EEJ is generated by the eastward electric field in the *E* region (Richmond, 1979). Figure 4b shows the day-longitude distribution of the TEC at 20°N geomagnetic latitude at 13–15 LT. The largest amplitudes of the TEC 6 day waves are seen at about ±20° geomagnetic latitudes. The 13–15 LT is chosen because the response of the Q6DW on the TEC is the largest at 13–15 LT

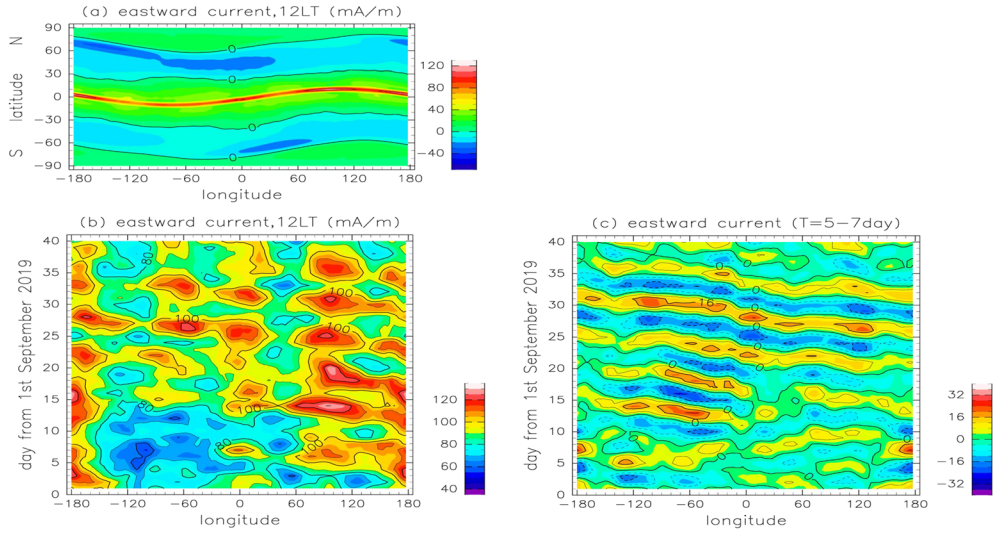

Figure 3. (a) Latitude-longitude distribution of the eastward current at 12 LT in September 2019. Units are mA/m. (b) Day-longitude distribution of the eastward current at 12 LT on the geomagnetic equator. Units are mA/m. (c) Variations with a period between 5 and 7 days in the eastward current at 12 LT.

(Yamazaki, 2018). Again, the westward moving structure of $s = 1$ with a period of 6 days is evident. Thus, the 6 day oscillation is dominant in the ionosphere during September 2019 as shown in Y20. Note that the EEJ, electric field, and TEC have the 6 day oscillation, even though the solar $F10.7$ flux and geomagnetic activity are held constant during the numerical simulation. This indicates that the 6 day oscillation in the ionosphere is caused by the atmospheric waves from below.

3.3. Neutral Atmosphere in the *E* Region

The neutral wind in the 110–120 km height region, where the neutral-plasma interaction processes are active, is examined here. Figure 5a shows the temporal variations in the meridional wind at 43°N and 90°E, averaged over the 110–120 km height range. The meridional wind velocity shows short-period fluctuations of up to ±150 m/s. The wind variations due to the planetary waves (periods >2 days) and tides (8, 12, and 24 hr periods) are dominant in the MLT. The wind variations do not have spectral peaks at 10, 16, and 36 hr. Thus, the meridional wind variations are decomposed into these four parts using a band-pass filter: (1) variations with periods longer than 36 hr (Figure 5b), (2) variations with periods between 16 and 36 hr (Figure 5c), (3) variations with periods between 10 and 16 hr (Figure 5d), and (4) variations with periods shorter than 10 hr (Figure 5e). In Figure 5b, variations with a period around 6 days are unclear, indicating that variations in the meridional wind due to the Q6DW are negligible in the midlatitude *E* region. The dominant component is the variations with periods between 10 and 16 hr (Figure 5d), which are mainly due to the semidiurnal tide.

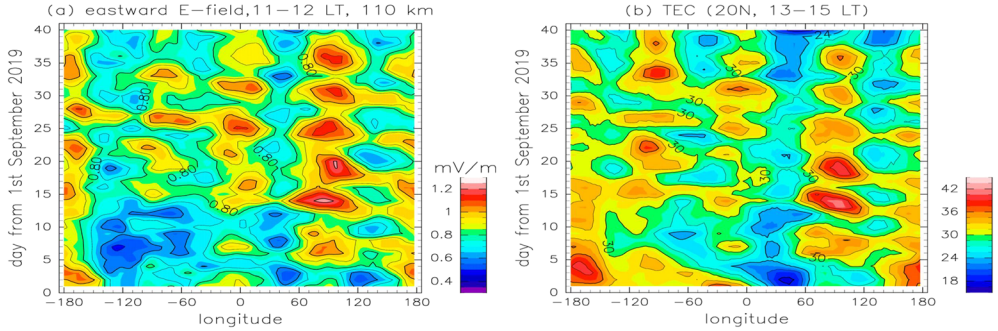

Figure 4. (a) Day-longitude distribution of the eastward electric field at 12 LT in low latitudes (±10° geomagnetic latitude). Units are mV/m. (b) Day-longitude distribution of the total electron content (TEC) at 13–15 LT at 20° geomagnetic N. Units are TECU.

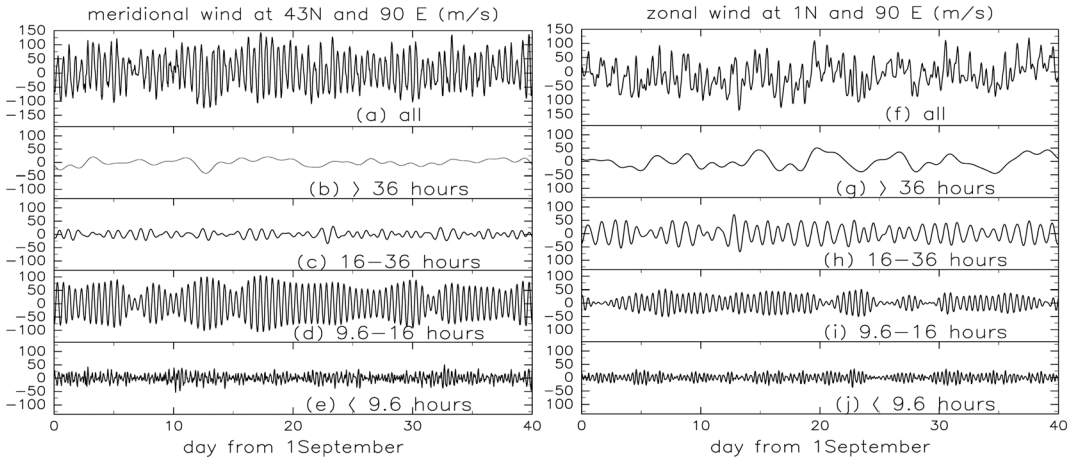

Figure 5. (a) Temporal variations in meridional wind at 43°N and 90°E from 1 September to 10 October 2019. The meridional wind is averaged between 110 and 120 km height. Units are m/s. (b) Temporal variations in meridional wind due to waves with periods longer than 36 hr. (c) Temporal variations in meridional wind with periods between 16 and 36 hr. (d) Temporal variations of meridional wind with periods between 9.6 and 16 hr. (e) Temporal variations with periods shorter than 9.6 hr. (f) As in Figure 5a but for the zonal wind at 1°N. (g) As in Figure 5b but for the zonal wind at 1°N. (h) As in Figure 5c but for the zonal wind at 1°N. (i) As in Figure 5d but for the zonal wind at 1°N. (j) As in Figure 5e but for the zonal wind at 1°N.

The range of the oscillation changes over time with a period of 5–6 days. For example, the 10–16 hr variations are amplified on 8, 13, 18, 24, and 30 September and 4 October. Variations with periods between 16 and 36 hr and with periods less than 10 hr are smaller than the 10–16 hr variations by a factor of 3–4. Figures S1a–S1e show the temporal variations in the zonal wind at 43°N and 90°E. The features of the zonal wind variations are similar to those of the meridional wind variations.

Similar analysis was performed on the zonal wind component near the equator (1°N and 90°E; Figures 5f–5j). The zonal wind variations due to the Q6DW are found in Figure 5g. The amplitude of the 10–16 hr variations (Figure 5i) is comparable to that of the 16–36 hr variations (Figure 5h), which are mainly due to the diurnal tide. The amplitude of the 10–16 hr variations is modulated with a period of 6 days, whereas the amplitude of the 16–36 hr variations is modulated with a period of 3–6 days. The temporal variations in the meridional wind near the equator are shown in Figures S1f–S1j. Again, the amplitude of the 10–16 hr variations is modulated with a period of 5–6 days. Figure S2 shows the 10–16 hr variations at different latitudes, where ~6 day modulations can also be found.

3.4. Excitation Mechanism of the 6 Day Oscillation of the EEJ

Our analysis for the temporal variations in the neutral wind implies that there are two excitation sources for the 6day oscillation of the EEJ. One is the 6day variations in the neutral wind due to Q6DW. The other is the modulation of the 10–16 hr variations with a period of 5–6 days. In order to examine the primary cause for the 6 day oscillation of the EEJ, we performed three additional numerical experiments. In these experiments, the neutral atmospheric part of GAIA (GCM) is decoupled from the ionospheric and electrodynamic parts of GAIA. Using the space-time spectral analysis, the neutral atmospheric temperature, wind, and composition are reconstructed with the wave component having zonal wave number from $s = -5$ to $s = 5$. In the first experiment (EXP1), the ionospheric and electrodynamics models are forced by the neutral atmosphere with the zonal wave number from $s = -5$ to $s = 5$. This means that the effect of the atmospheric waves with relatively small spatial scales ($|s| > 5$) on the ionosphere is excluded. Moreover, the effect of the feedback processes from the ionosphere to the neutral atmosphere, such as the ion drag force, is omitted. In the second experiment (EXP2), the neutral atmosphere is reconstructed by the Q6DW (westward moving $s = 1$ components with a period of 5–7 days) and 40 day means (averaged from 1 September to 10 October) of the zonal mean and tidal components of $|s| \leq 5$. This means that the day-to-day variations in the ionosphere are only generated by the Q6DW. In the third experiment (EXP3), the atmospheric waves with periods longer than 36 hr for $|s| \leq 5$ are removed. Day-to-day variations in the ionosphere are generated by variations in the atmospheric waves with periods shorter than 36 hr. Namely, the effects of the temporal

Table 1
A Brief Description of the Three Additional Numerical Experiments

	GAIA simulation	EXP1	EXP2	EXP3
Neutral-plasma interaction	○	One way	One way	One way
Zonal wave number	0–42	0–5	0–5	0–5
Periods	All	All	5–7 days	<36 hr

variations in the tides (24, 12, 8, and 6 hr) on the ionosphere are considered, whereas the effect of the Q6DW is removed. A brief summary of EXP1–EXP3 is given in Table 1. The three experiments are conducted from 1 September to 10 October 2019. By comparing the 6 day oscillation of the EEJ in the three experiments, we can identify the excitation source of the 6 day oscillation of the EEJ.

Figure 6a shows the day-longitude distribution of the EEJ obtained by EXP1. The EEJ has the wave 4 longitudinal structure with maxima at 0°E, 90°E, 180°E, and 90°W. The westward moving component of $s = 1$ with a period of 6 days is significant after 10 September (Figure 6d). These features of the EEJ are quite similar to those obtained by the original GAIA simulation. This result indicates that the 6 day oscillation of the EEJ is generated by the large-scale waves ($|s| \leq 5$).

The day-longitude distribution of the EEJ simulated by EXP2 is presented in Figures 6b and 6e. The amplitude of the wave 4 structure of the EEJ is reduced, and day-to-day variations in the EEJ are much weaker than those in EXP1. The westward moving component of $s = 1$ with a period of 6 days is visible in Figure 6e; however, the amplitude of the 6 day oscillation is only 2–3 mA/m, which is weaker than that in EXP1 and the original GAIA simulation by a factor of 6–8.

The day-longitude distribution of the EEJ obtained by EXP3 is quite similar to that in EXP1 and the original GAIA simulation (Figures 6c and 6f). This indicates that the 6 day oscillation of the EEJ is primarily generated by the planetary-scale waves with periods less than 36 hr. Day-to-day variations in the TEC simulated by EXP1, EXP2, and EXP3 are shown in Figures 7. Note that day-to-day variations in EXP1 and EXP3 agree well with those in the original GAIA simulation.

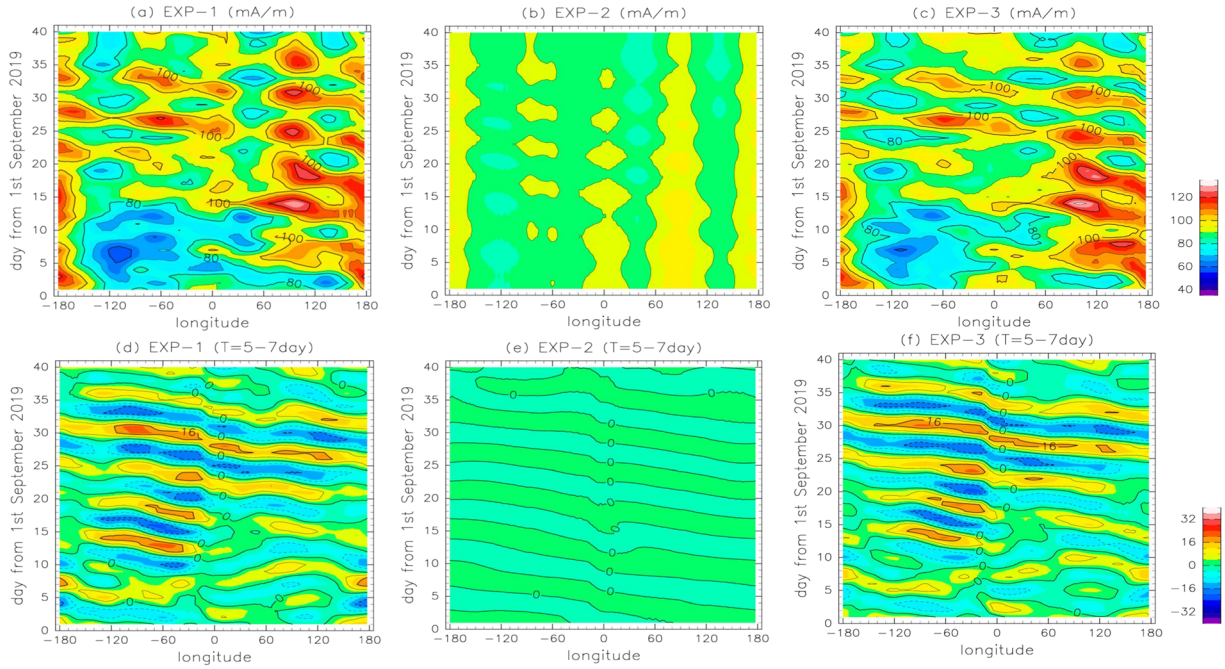

Figure 6. (a) Day-longitude distribution of the eastward current at the geomagnetic equator at 12 LT obtained by EXP1. Units are mA/m. Contour intervals of black lines are 10 mA/m. (b) As in Figure 6a but for EXP2. (c) As in Figure 6a but for EXP3. (d) The 5–7 day variations of the eastward current obtained by EXP1. Contour intervals of black lines are 4 mA/m. (e) As in Figure 6d but for EXP2. (f) As in Figure 6e but for EXP3.

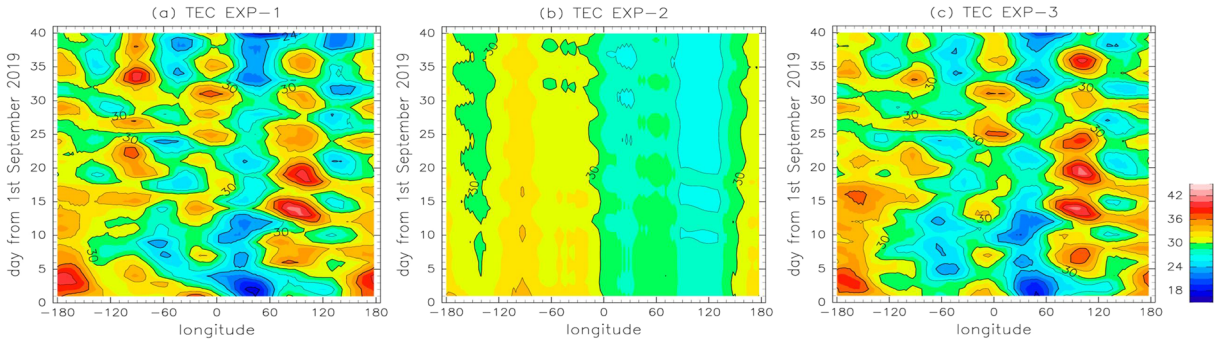

Figure 7. (a) Day-longitude distribution of the TEC at 20° geomagnetic N latitude at 13–15 LT simulated by EXP1. Units are TEC unit. (b) As in Figure 7b but for EXP2. (c) As in Figure 7a but for EXP3.

3.5. The 10–16 hr Variations

To investigate the dominant periods of the planetary-scale waves in more detail, the space-time spectral analysis was performed. Figure 8a shows the frequency-zonal wave number distribution of spectral density of the meridional wind at 43°N averaged between 110 and 120 km height. A narrow band of enhanced spectral density is found at ω = 2/day (12 hr period) with s = − 2 ~ 4. The maximum is located at ω = 2 with $s = 2$, which is due to the migrating semidiurnal tide (SW2). Other distinct peaks are evident at ω = 1 with $s = 1$ (migrating diurnal tide, DW1) and at ω = 3 with $s = 3$ (migrating terdiurnal tide). It is important that spectral peaks are found at ω = 1.833 (about 13 hr period) with s = − 1 ~ 1 and 3 and at ω = 2.167 (about 11 hr period) with s = 0,3,and 4. In these waves, westward moving component of $s = 1$ with ω = 1.833 (W1_13h) and westward moving component of s = 3 with ω = 2.167 (W3_11h) are larger. These two waves are considered to be the secondary waves generated through the nonlinear interaction between the Q6DW and SW2 (e.g., Gan et al., 2017). The wind variations due to Q6DW (u_{6d}) and SW2 (u_{sw2}) are expressed as Equations 1 and 2, respectively:

$$u_{6d} = A_1 \cos(x + 0.167\Omega Ut + \phi_1) \tag{1}$$

$$u_{sw2} = A_2 \cos(2x + 2\Omega Ut + \phi_2) \tag{2}$$

where x,Ut,and Ω are the longitude, universal time (in hours), and 2π/24, respectively. A_k and ϕ_k are the wave amplitude and phase, respectively. The generation of W1_13h and W3_11h through the nonlinear interaction is described in Equation 3:

$$\begin{aligned} &A_1 \cos(x + 0.167\Omega Ut + \phi_1) \times A_2 \cos(2x + 2\Omega Ut + \phi_2) \\ &= \frac{A_1 A_2}{2}[\cos(x + 1.833\Omega Ut - \phi_1 + \phi_2) + \cos(3x + 2.167\Omega Ut + \phi_1 + \phi_2)] \end{aligned} \tag{3}$$

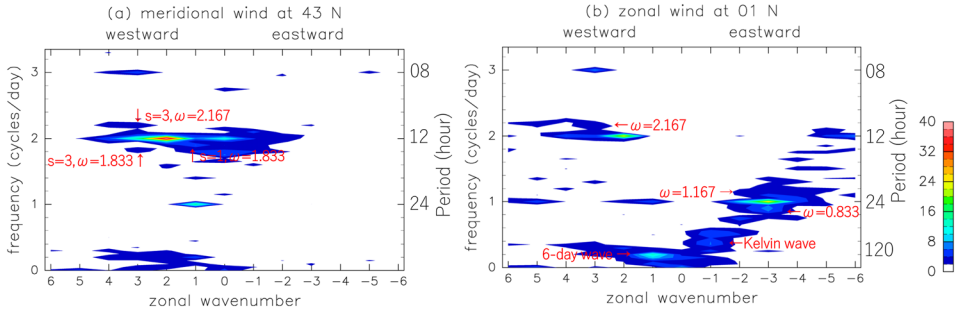

Figure 8. (a) Zonal wave number-frequency spectral distribution of the spectral density of the meridional wind component at 43°N averaged from 110 to 120 km height (10–30 September 2019). Positive and negative values of zonal wave number indicate westward and eastward moving waves, respectively. (b) As in Figure 8a but for the zonal wind component at 01° N.

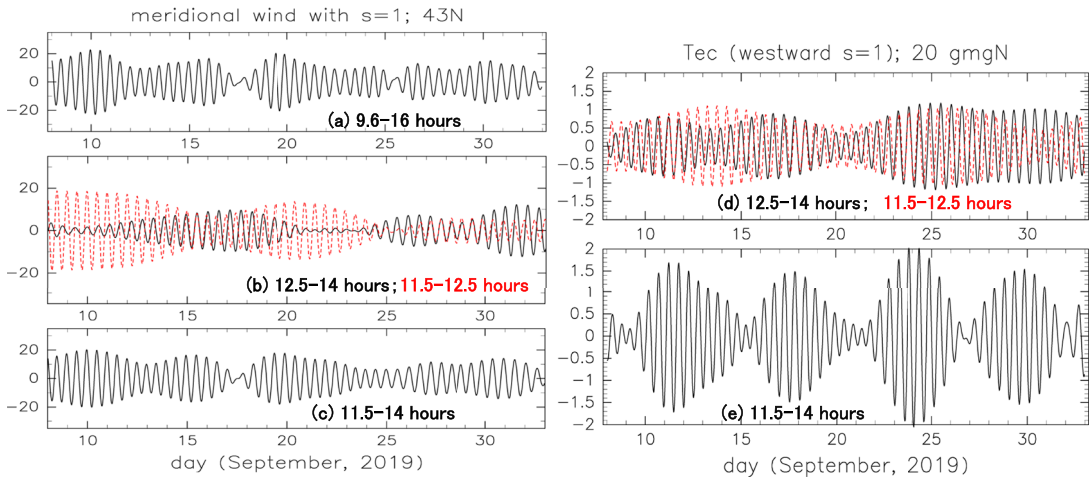

Figure 9. (a) Temporal variations in meridional wind with $s = 1$ at 43°N and 90°E. Variations due to the waves with periods between 9.6 and 16 hr are shown. The meridional wind is averaged between 110 km and 120 km height. (b) Black solid (red broken) line shows temporal variations with periods between 12.5 and 14 (11.5 and 12.5) hr. (c) Black solid line is superposition of back solid line and red broken lines of Figure 9b. (d) Black solid (red broken) line shows temporal variations of westward moving $s = 1$ components of TEC with periods between 12.5 and 14.0 (11.5 and 12.5) hr at 20°N geomagnetic latitude and 90°E. Units are TECU. (e) Black solid line is superposition of these two components ($s = 1$, 11.5–14.0 hr).

Furthermore, westward moving component of $s = 3$ with $\omega = 1.833$ is the secondary wave by the nonlinear interaction between the Q6DW and SW4 (westward moving semidiurnal tide with $s = 4$), whereas $s = 0$ component with $\omega = 1.833$ is the secondary wave by the nonlinear interaction between the Q6DW and SW1 (westward moving semidiurnal tide with $s = 1$). The secondary waves generated by the Q6DW and tides are described in detail by Forbes and Zhang (2017). In the following, the behaviors of W1_13h and W3_11h, which are the largest in the secondary waves, are examined.

Figure 9a shows 9.6–16 hr variations in the westward moving $s = 1$ component of the meridional wind at 43°N and 90°E. The meridional wind variations are modulated with a period of about 5–6 days. The black and red lines in Figure 9b show temporal variations with periods from 12.5 and 14 hr (W1_13h) and variations with periods from 11.5 and 12.5 hr (SW1), respectively. Because the simulation data are sampled every 30 min, we can distinguish the wave with a period of 13 hr (W1_13h) from the SW1 (12 hr period) using a 3 day window. Neither of the two waves shows 6 day periodicity. However, their superposition reveals a modulation with a period of 6 days (Figure 9c), because the two components are in phase every 6 days. Thus, the 6 day periodicity in Figure 9a is primarily explained by the interference of W1_13h and SW1.

A similar analysis was conducted on the westward moving $s = 3$ component with periods from 9.6 to 16 hr. The westward moving $s = 3$ component also shows variations with a period about 6 days (Figure 10a). Figure 10b shows the temporal variations with periods from 12.5 to 14.0 hr (W3_13h), whereas Figure 10c shows the variations with periods from 11.5 to 12.5 (SW3; red line) and with periods from 10.0 to 11.5 hr (black line; W3_11h), respectively. During 13–25 September, the amplitude of W3_11h is larger than that of W3_13h, and day-to-day variations in the westward moving $s = 3$ component are primarily explained by the superposition of SW3 and W3_11h. On the other hand, W3_13h is not negligible before 13 September and after 25 September. The interference between SW3 and W3_11h (as well as between SW3 and W3_13h) is also found at other latitudes and in the zonal wind component (not shown).

Figures 11a and 11b show the amplitudes of the zonal and meridional wind components of the W1_13h averaged over 10 to 30 September. The maxima of 8–13 m/s are located at ±60–70° latitude and 110–120 km height. Secondary peaks of the meridional wind (6 m/s) appear at ±20° latitude and 120–140 km height. The amplitude below 80 km height is negligibly small, whereas the amplitude above 150 km height decreases with increasing height. Day-to-day variations of the W1_13h amplitude (the meridional wind component) at 115 km height is shown in Figure 12a. Day-to-day variations in the W1_13h amplitude are prominent. The amplitude at high latitudes in the NH has a peak of 23 m/s on 14–19 September, whereas the amplitude at middle and high latitudes in the SH is enhanced after 20 September. The amplitudes of the W3_11h in the zonal and meridional wind components are shown in Figures 11c and 11d, respectively.

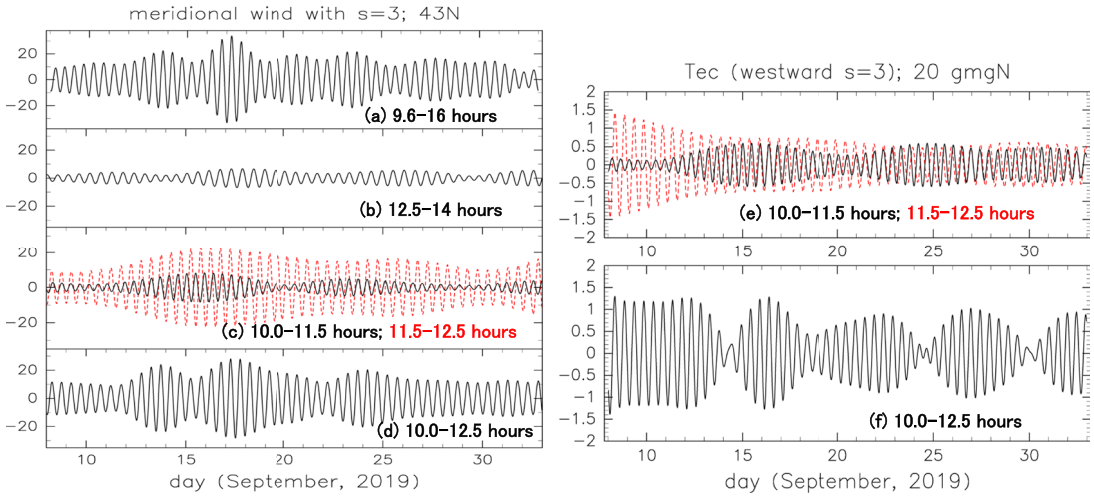

Figure 10. (a) Temporal variations in the meridional wind with $s = 3$ at 43°N and 90°E. Variations due to waves with periods between 9.6 and 16 hr are shown. The meridional wind is averaged between 110 and 120 km height. (b) Temporal variations with periods between 12.5 and 14 hr. (c) Black solid (red broken) line shows temporal variations with periods between 10.0 and 11.5 (11.5 and 12.5) hr. (d) Black solid line is superposition of back solid line and red broken line of Figure 10c. (e) Temporal variations in TEC with $s = 3$ at 20° geomagnetic N and 90°E. Black solid (red broken) line shows variations with periods between 10.0 and 11.5 (11.5 and 12.5) hr. (f) Black line is superposition of black solid and red broken line of Figure 10e.

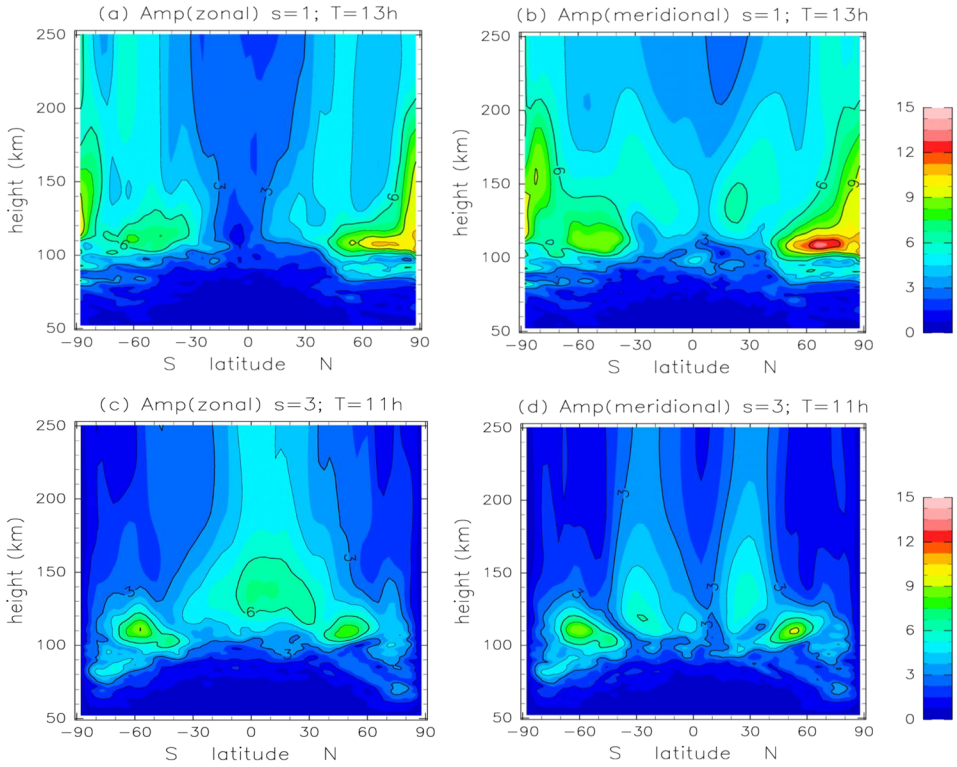

Figure 11. (a) Height-latitude distribution of the W1_13h amplitude in the zonal wind component averaged from 10 to 30 September 2019. Units are m/s. (b) As in Figure 11b but for the meridional wind component. (c) Height-latitude distribution of the W3_11h amplitude in the zonal wind averaged from 10 to 30 September 2019. (d) As in Figure 11c but for the meridional component.

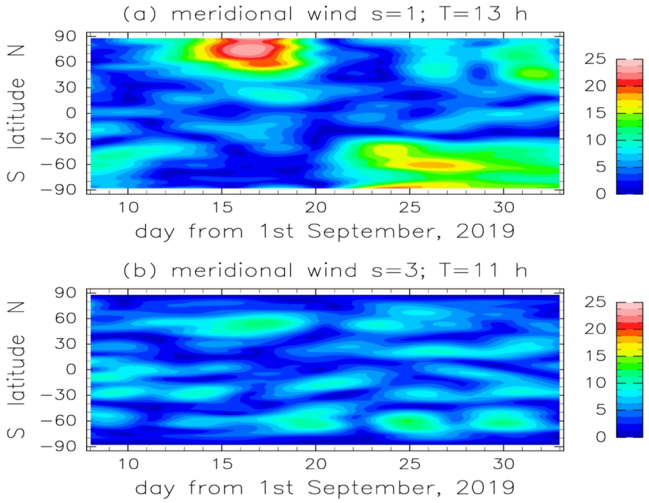

Figure 12. (a) Latitude-time distribution of the W1_13h amplitude in the meridional wind at 115 km height. Units are m/s. (b) As in Figure 12a but for the W3_11h amplitude.

The amplitudes in the zonal and meridional winds have maxima of 10 m/s at ±50–60° latitudes and 110–120 km heights. A secondary peak of the zonal wind amplitude (7.5 m/s) is found near the equator at 130 km height, whereas that of the meridional wind amplitude (6 m/s) appears at ±20–30° latitudes. Day-to-day variations in W3_11h indicate that the amplitude in the NH (SH) is enhanced on 15–20 (20–30) September (Figure 12b).

The spectral density distribution of the zonal wind near the equator is shown in Figure 8b. The spectral density is larger at ω = 1/day (24 hr period) than at ω = 2/day (12 hr period). In particular, strong peaks are found at ω = 1 with eastward moving $s = -3$. Peaks associated with the Q6DW (ω = 0.167 and $s = 1$) and Ultra Fast Kelvin wave (ω = 0.3 – 0.5 and $s = -1$) are visible. Distinct peaks at ω = 0.833 (29 hr period) and ω = 1.167 (21 hr period) with s = − 2 to − 4 are considered to be the secondary waves resulting from the nonlinear interaction between the Q6DW and the diurnal tides. The spectral peak due to the wave at ω = 0.833 with $s = -3$ (E3_29h) is the largest in the secondary waves and is generated by the interaction between the Q6DW and eastward moving diurnal tide with $s = -2$ (DE2). Figure S4 shows the height-latitude distribution of the E3_29h amplitude. The amplitude of the zonal wind E3_29h has the maximum of 10 m/s at the equator and 110 km height, whereas the amplitude of the meridional wind E3_29h is less than 5 m/s. The zonal wind variations due to E3_29h also affect the 6-day variation in the ionosphere. Furthermore, a spectral peak due to W3_11h (ω 2.167 and $s = 3$) is found.

3.6. Semidiurnal Variation in the Ionosphere

It is considered that the neutral wind variations, such as SW1, SW2, SW3, W1_13h and W3_11h, influence the temporal variations in the electron density. Let us first examine the TEC variations associated with W1_13h and SW1. Black and red lines in Figure 9d indicate the westward moving $s = 1$ component of the TEC variations with periods between 12.5 and 14.0 hr and with periods between 11.5 and 12.5 hr, respectively. The amplitude of the both variations ranges from 0.3 to 1.2 TEC unit. It is seen that neither variation has clear 6 day periodicity, whereas the superposition of the two has a 6 day oscillation. This means that the amplitude of the semidiurnal variation (11.5–14.0 hr) in TEC is modulated with a 6 day period due to the interference of W1_13h and SW1. The westward moving $s = 3$ component also has similar feature. Namely, the superposition of the TEC variations with periods between 10.5 and 11.5 hr and with periods between 11.5 and 12.5 hr shows clear 6-day variation (Figures 10e and 10f).

3.7. Variations in the Fixed Local Time Frame

As presented in Figures 3, 4, 6, and 7, the 6 day oscillation in the EEJ and TEC at fixed local times has the westward moving s = 1 structure, which is consistent with Swarm observations during September 2019 (Y20). As demonstrated in 3.4, these 6 day ionospheric oscillations are not due to the Q6DW with $s = 1$ but due to 10–14 hr waves with $s = 1$ and $s = 3$. In this subsection, we explain how the 10–14 hr waves produce westward moving $s = 1$ ionospheric perturbations in the fixed LT frame.

Let us consider the neutral wind variations due to Q6DW, W1_13h, and W3_11h at a fixed LT. The relation between UT and LT is expressed in Equation 4, so that the wind variation due to the Q6DW (1) at a fixed LT is described as Equation 5:

$$x + \Omega \mathrm{Ut} = \Omega \mathrm{Lt} \tag{4}$$

$$u_{6d} = A_1 \cos(0.833x + 0.167\Omega Lt + \phi_1) \tag{5}$$

The wind variation due to W1_13h is described in Equation 6:

$$u_{w1\_13} = \mathrm{A}_3 \cos(x + 1.833\Omega Ut + \phi_3) \tag{6}$$

Using Equation 4, the wind variation of W1_13h at a fixed LT is expressed in equation 7:

$$u_{w1\_13} = \mathrm{A}_3 \cos(0.833x + 0.167\Omega Lt - \phi_3) \tag{7}$$

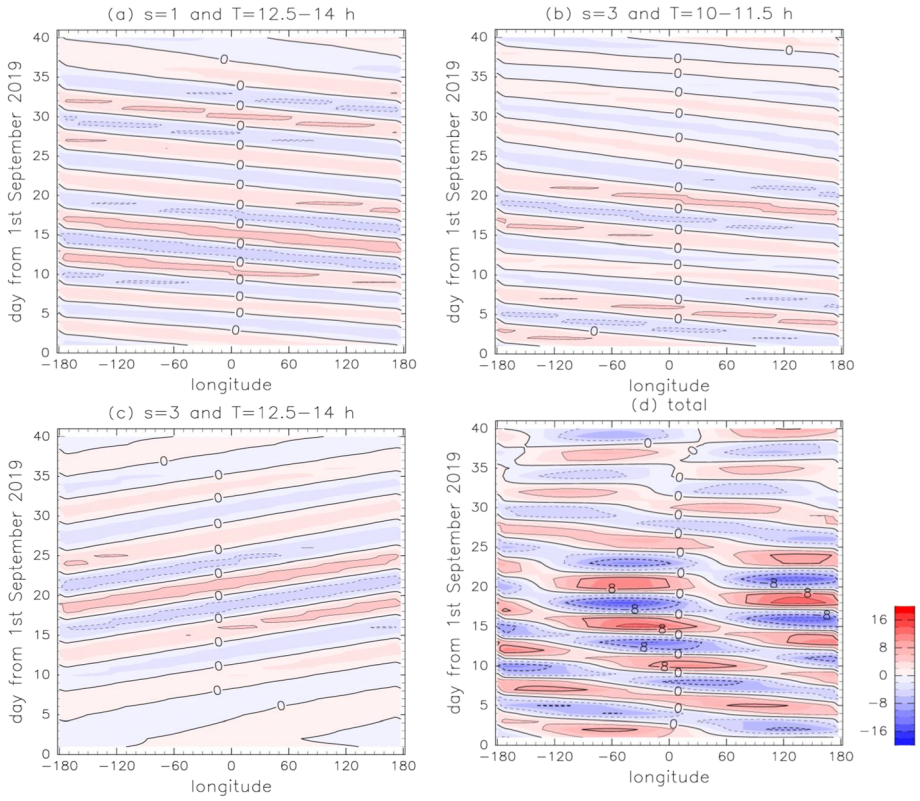

Figure 13. (a) Day-longitude distribution of meridional wind at 43°N and 12 LT (fixed local time framework) due to the W1_13h. Units are m/s. (b) As in Figure 13a but for the W3_11h. (c) As in Figure 13a but for the W3_13h. (d) Day-longitude distribution of superposition of all three waves.

By comparing Equations 5 and 7, it is obvious that the time-longitude structure of the wind variation due to the Q6DW is the same with that due to the W1_13h. Figures S5a and S5b show the day–longitude wind variations due to the Q6DW and W1_13h at 12 LT, respectively.

Similarly, the wind variation due to the W3_11h is described in Equation 8. The wind variation due to the W3_11h at the fixed LT (Figure S5c) has the same longitudinal dependence as Q6DW and W1_13h.

$$u_{w3\_11} = \mathrm{A}_4 \cos(3x + 2.167\Omega Ut + \phi_4) = A_4 \cos(0.833x + 0.167\Omega Lt + \phi_4) \tag{8}$$

On the other hand, the wind variations due to the W1_11h and W3_13h are described in Equations 9 and 10, respectively.

$$u_{w1\_11} = A_5 \cos(x + 2.167\Omega Ut + \phi_5) = A_5 \cos(-1.167x + 0.167\Omega Lt + \phi_5) \tag{9}$$

$$u_{w3\_13} = \mathrm{A}_6 \cos(3x + 1.833\Omega Ut + \phi_6) = \mathrm{A}_6 \cos(-1.167x + 0.167\Omega Lt - \phi_6) \tag{10}$$

The wind variations due to the W1_11h and W3_13h at a fixed LT have eastward moving structure (Figures S4d and S4e), which is quite different from that of the Q6DW, W1_13h, and W3_11h.

Based on these results, we can conclude that the wind variations due to the Q6DW, W1_13h, and W3_11h at a fixed LT have the westward moving $s = 1$ structure with a period of 6 days. Furthermore, using the same procedure, it can be shown that the wind variations due to W3_21h and S0_29h, which are the secondary waves from the nonlinear interaction between the Q6DW and the migrating diurnal tide, also have the westward moving $s = 1$ structure with a period of 6 days in the fixed LT frame.

Figures 13a and 13b show the day-longitude distributions of the meridional wind associated with the W1_13h and W3_11h at 43°N and 110–120 km height, as derived from GAIA at 12 LT. As shown before, the wind variations due to these two waves have the westward moving $s = 1$ structure with a period of

6 days. On the other hand, the meridional wind variation due to the W3_13h at 12 LT, shown in Figure 13c, indicates eastward moving structure having $s = 1$. Figure 13d shows the day-longitude distribution of the meridional wind obtained by the superposition of W1_13h, W3_11h, and W3_13h at 12 LT. The westward moving $s = 1$ structure with a period of 6 days is dominant in Figure 13d. Based on the results obtained in the current study, we can conclude that the 6-day variation with $s = 1$ in the ionosphere is primarily caused by the neutral wind variation due to superposition of the secondary waves generated by the nonlinear Q6DW-tide interaction, such as the W1_13, W3_11h, and W3_13h. Similar day-longitude distributions of the neutral wind are found at other latitudes.

The amplitude of the 6-day variation in the neutral wind due to the superposition of the W1_13, W3_11h, and W3_13h depends on longitude. On 10–20 September, the 6-day variation in the neutral wind is enhanced at 90–30°W longitudes. A strong 6-day variation in the EEJ and TEC on 10–20 September also occurs at 90–30°W longitudes. This suggests that the longitudinal dependence of the 6-day variation in the EEJ and TEC is caused by the longitudinal dependence of the amplitude of the neutral wind variation.

4. Discussion

Pancheva et al. (2010) showed that the Q6DW is active during equinoxes in both hemispheres reaching the maximum at 105–110 km height. Using the Aura/MLS, Yamazaki (2018) investigated the climatology of the Q6DW during a period from 2004 to 2017. The Q6DW amplitude of the geopotential height at a height of 97 km ranges from 0.15 to 0.3 km. The Q6DW amplitude in September 2019 exceeds 0.4 km and is the largest since 2004. Thus, the Q6DW event in September 2019 is very strong.Using the TIME-GCM, Gan et al. (2017) studied the 6 day oscillation in the ionosphere and its relation with the Q6DW. They showed that the W0_21h, W2_29h, W1_13h, and W3_11h, which are generated by the nonlinear interaction between the Q6DW and the DW1/SW2, played an important role on the 6-day variation in the ionosphere, which is consistent with the present results. The maxima of the W1_13h and W3_11h amplitudes simulated by Gan et al. (2017) are 3–5 m/s and are smaller than those simulated in this study by a factor of 3–4. The Q6DW amplitude is exceptionally large during September 2019, and the amplitude of the SW2 at 100–120 km height in this study (Figures S3) is 40–60 m/s, larger than that in Gan et al. (2017) by 5–10 m/s. Thus, the larger amplitudes of the parent waves (the Q6DW and SW2) are likely the reason for the larger secondary waves in this study. On the other hand, the amplitudes of the W0_21h and W2_29h simulated in this study are smaller than those in Gan et al. (2017). The DW1 amplitude at 100–120 km in this study is also smaller than that in Gan et al. (2017). Therefore, the smaller amplitudes of the secondary waves (W0_21h and W2_29h) in this study are probably due to the smaller amplitude of the DW1.

Pedatella et al. (2012) reported that eastward moving waves with periods of 21 and 29 hr at low latitudes, which are generated by the nonlinear interaction between the Q6DW and eastward moving diurnal tides. The amplitude of these waves is about 10 m/s, and is consistent with the present result.

Next, we compare the 6-day variation in the EEJ in September 2019 with the 6-day variation in other years. Yamazaki (2018) investigated the behavior of the 6day variation in the EEJ for five events (September 2006, May 2007, September 2007, August 2010, and September 2016). In these five events, the westward moving $s = 1$ structure with a period of 6 days is not as clear as the September 2019 event, and the amplitude of the 6day variation in the EEJ has a more pronounced longitudinal dependence. For example, the 6day variation in EEJ in September 2006 event is clearly seen at 180–210°E longitudes but nearly absent at 30–60°E longitude. For the September 2006 event, the amplitude of the Q6DW in geopotential height is ~0.2 km at 95 km height, which is half the amplitude of the September 2019 event. From this, it is expected that the amplitudes of the secondary waves (W1_13h and W3_11h) in the September 2006 event are much smaller than those in the September 2019 event. The smaller amplitudes of the secondary waves could be the reason for the unclear westward moving $s = 1$ structure in the EEJ for the September 2006 event. The evaluation of the secondary waves during other Q6DW events and their impacts on the 6 day ionospheric oscillation requires further studies.

5. Concluding Remarks

Using an atmosphere-ionosphere coupled model (GAIA), the excitation mechanism of the 6-day variations in the EEJ and TEC has been investigated. The main results are as follows:

1. The Q6DW in the stratosphere and mesosphere is extremely enhanced during the SSW event in September 2019. The Q6DW amplitude reaches its maximum at 95 km height and decreases with increasing height at 95–120 km height. The Q6DW amplitude in the zonal wind at 95 and 110 km heights is 27 and 20 m/s, respectively. The Q6DW amplitude in the zonal wind above 150 km is less than 10 m/s.
2. By a series of numerical experiments, we demonstrate that the 6-day variations in the EEJ and TEC are not caused by the neutral wind variation due to the Q6DW but caused by waves with periods of 11–14 hr. The amplitude of the 11–14 hr waves in neutral winds is modulated with a period of 6 days and plays an important role on the excitation of the 6-day variation in the ionosphere. Specifically, the W1_13h and W3_11h waves, which are the secondary waves generated by the nonlinear interaction between the Q6DW and SW2, are important.
3. At the fixed local time, the wind variations due to the W1_13h and W3_11h have the westward moving $s = 1$ structure with a period of 6 days. This is the reason why the EEJ and TEC in the fixed LT frame show 6-day variations with the westward moving $s = 1$ component.
4. The interference of the secondary waves induces a longitudinal asymmetry in the amplitude of the 6-day variation in the neutral wind. This, in turn, leads to a longitudinal asymmetry in the magnitude of the ionospheric 6-day variation.

In this study, we showed the excitation mechanism of the 6-day variation in the ionosphere. However, the excitation mechanism of the Q6DW in the stratosphere and mesosphere remains to be identified. The reason why the Q6DW in September 2019 is extremely enhanced is also unclear. Furthermore, additional GAIA simulations for other years are desirable to study the interannual variability of the Q6DW activity and its relation with the 6-day variation in the ionosphere. These are subjects of future studies.

Data Availability Statement

The simulation data used in this study are available from GFZ Data Services (https://doi.org/10.5880/GFZ.2.3.2020.004).

Acknowledgments

The numerical simulation was mainly performed using the computer systems at Research Institute for Information Technology of Kyushu University and at National Institute of Information and Communications Technology, Japan. This project was supported by JSPS and DFG under the Joint Research Projects-LEAD with DFG (JRPs-LEAD with DFG). This work was also supported in part by ESA through contract 4000126709/19/NL/IS "VERA". The GFD/DENNOU library was used to produce the figures. The JRA-55 meteorological reanalysis data sets are provided by the Japan Meteorological Agency (JMA).

References

Forbes, J. M., & Zhang, X. (2017). The quasi-6 day wave and its interactions with solar tides. *Journal of Geophysical Research: Space Physics*, *122*, 4764–4776. https://doi.org/10.1002/2017ja023954

Fuller-Rowel, T. J., Wu, F., Akmaev, R. A., Fang, T.-W., & Araujo-Pradere, E. A. (2010). A Whole Atmosphere Model simulation of the impact of a sudden stratospheric warming on thermosphere dynamics and electro-dynamics. *Journal of Geophysical Research*, *115*, A00G08. https://doi.org/10.1029/2010JA015524

Gan, Q., Oberheide, J., Yue, J., & Wang, W. (2017). Short-term variability in the ionosphere due to the nonlinear interaction between the 6 day wave and migrating tides. *Journal of Geophysical Research: Space Physics*, *122*, 8831–8846. https://doi.org/10.1002/2017JA023947

Gan, Q., Wang, W., Yue, J., Liu, H., Chang, L. C., Zhang, S., & Du, J. (2016). Numerical simulation of the 6 day wave effects on the ionosphere: Dynamo modulation. *Journal of Geophysical Research: Space Physics*, *121*, 10–103. https://doi.org/10.1002/2016JA022907

Gelaro, R., McCarty, W., Suárez, M. J., Todling, R., Molod, A., Takacs, L., et al. (2017). The Modern-Era Retrospective Analysis for Research and Applications, Version 2 (MERRA-2). *Journal of Climate*, *30*(14), 5419–5454. https://doi.org/10.1175/jcli-d-16-0758.1

Gu, S. Y., Liu, H. L., Li, T., Dou, X. K., Wu, Q., & Russell, J. M. (2014). Observation of the neutral-ion coupling through 6 day planetary wave. *Journal of Geophysical Research: Space Physics*, *119*, 10,376–10,383. https://doi.org/10.1002/2014JA020530

Hayashi, Y. (1971). A Generalized Method of Resolving Disturbances into Progressive and Retrogressive Waves by Space Fourier and Time Cross-Spectral Analyses. *Journal of the Meteorological Society of Japan. Ser. II*, *49*(2), 125–128. https://doi.org/10.2151/jmsj1965.49.2_125

Hirota, I., & Hirooka, T. (1984). Normal mode Rossby waves observed in the upper stratosphere. Part I: First symmetric modes of zonal wavenumbers 1 and 2. *Journal of the Atmospheric Sciences*, *41*(8), 1253–1267.

Jin, H., Miyoshi, Y., Fujiwara, H., & Shinagawa, H. (2008). Electrodynamics of the formation of ionospheric wave number 4 longitudinal structure. *Journal of Geophysical Research*, *113*, A09307. https://doi.org/10.1029/2008JA013301

Jin, H., Miyoshi, Y., Fujiwara, H., Shinagawa, H., Terada, K., Terada, N., et al. (2011). Vertical connection from the tropospheric activities to the ionospheric longitudinal structure simulated by a new Earth's whole atmosphere-ionosphere coupled model. *Journal of Geophysical Research*, *116*, A01316. https://doi.org/10.1029/2010JA015925

Kobayashi, S., Ota, Y., Harada, H., Ebita, A., Moriya, M., Onoda, H., et al. (2015). The JRA-55 reanalysis: General specifications and basic characteristics. *Journal of the Meteorological Society of Japan*, *93*(1), 5–48. https://doi.org/10.2151/jmsj.2015-001

Liu, G., Immel, T. J., England, S. L., Kumar, K. K., & Ramkumar, G. (2010). Temporal modulations of the longitudinal structure in *F*2 peak height in the equatorial ionosphere as observed by COSMIC. *Journal of Geophysical Research*, *115*, A04303. https://doi.org/10.1029/2009JA014829

Liu, H.-L., Wang, W. A., Richmond, D., & Roble, R. G. (2010). Ionospheric variability due to planetary waves and tides for solar minimum conditions. *Journal of Geophysical Research*, *115*, A00G01. https://doi.org/10.1029/2009JA015188

Madden, R., & Julian, P. (1972). Further evidence of global-scale 5-day pressure waves. *Journal of the Atmospheric Sciences*, *29*(8), 1464–1469. https://doi.org/10.1175/1520-0469(1972)029<1464:FEOGSD>2.0.CO;2

Miyoshi, Y. (1999). Numerical simulation of the 5-day and 16-day waves in the mesopause region. *Earth, Planets and Space*, *51*(7–8), 763–772. https://doi.org/10.1186/BF03353235

Miyoshi, Y., & Fujiwara, H. (2003). Day-to-day variations of migrating diurnal tide simulated by a GCM from the ground surface to the exobase. *Geophysical Research Letters*, *30*(15), 1789. https://doi.org/10.1029/2003GL017695

Miyoshi, Y., & Fujiwara, H. (2006). Excitation mechanism of intraseasonal oscillation in the equatorial mesosphere and lower thermosphere. *Journal of Geophysical Research*, *111*, D14108. https://doi.org/10.1029/2005JD006993

Miyoshi, Y., Fujiwara, H., Jin, H., Shinagawa, H., & Liu, H. (2012). Numerical simulation of the equatorial wind jet in the thermosphere. *Journal of Geophysical Research*, *117*, A03309. https://doi.org/10.1029/2011JA017373

Miyoshi, Y., & Hirooka, T. (1999). A numerical experiment of excitation of the 5-day wave by a GCM. *Journal of the Atmospheric Sciences*, *56*(11), 1698–1707. https://doi.org/10.1175/1520-0469(1999)056<1698:ANEOEO>2.0.CO;2

Miyoshi, Y., & Hirooka, T. (2003). Quasi-biennial variation of the 5-day wave in the stratosphere. *Journal of Geophysical Research*, *108*(D19). https://doi.org/10.1029/2002jd003145

Miyoshi, Y., Pancheva, D., Mukhtarov, P., Jin, H., Fujiwara, H., & Shinagawa, H. (2017). Excitation mechanism of non-migrating tides. *Journal of Atmospheric and Solar-Terrestrial Physics*, *156*, 24–36. https://doi.org/10.1016/j.jastp.2017.02.012

Pancheva, D., Mukhtarov, P., Andonov, B., & Forbes, J. M. (2010). Global distribution and climatological features of the 5–6-day planetary waves seen in the SABER/TIMED temperatures (2002–2007). *Journal of Atmospheric and Solar-Terrestrial Physics*, *72*(1), 26–37. https://doi.org/10.1016/j.jastp.2009.10.005

Pedatella, N. M., Liu, H.-L., & Hagan, M. E. (2012). Day-to-day migrating and nonmigrating tidal variability due to the six-day planetary wave. *Journal of Geophysical Research*, *117*, A06301. https://doi.org/10.1029/2012JA017581

Richmond, A. D. (1979). Ionospheric wind dynamo theory: A review. *Journal of geomagnetism and geoelectricity*, *31*(3), 287–310. https://doi.org/10.5636/jgg.31.287

Riggin, D. M., Liu, H.-L., Lieberman, R. S., Roble, R. G., Russell Iii, J. M., Mertens, C. J., et al. (2006). Observations of the 5-day wave in the mesosphere and lower thermosphere. *Journal of Atmospheric and Solar-Terrestrial Physics*, *68*(3–5), 323–339. https://doi.org/10.1016/j.jastp.2005.05.010

Salby, M. L. (1981). Rossby normal modes in nonuniform background configurations. Part II. Equinox and solstice conditions. *Journal of the Atmospheric Sciences*, *38*(9), 1827–1840. https://doi.org/10.1175/1520-0469(1981)038<1827:RNMINB>2.0.CO;2

Shinagawa, H. (2009). Ionosphere simulation. *Journal of the National Institute of Information and Communication Technology*, *56*(1-4), 199–207. https://www.nict.go.jp/publication/shuppan/kihou-journal/journa-vol56no1_4.html

Takahashi, H., Wrasse, C. M., Pancheva, D., Abdu, M. A., Batista, I. S., Lima, L. M., et al. (2006). Signatures of 3–6 day planetary waves in the equatorial mesosphere and ionosphere. *Annales de Geophysique*, *24*(12), 3343–3350. https://doi.org/10.5194/angeo-24-3343-2006

Wu, D., Hays, P., & Skinner, W. (1994). Observations of the 5-day wave in the mesosphere and lower thermosphere. *Geophysical Research Letters*, *21*(24), 2733–2736. https://doi.org/10.1029/94GL02660

Yamazaki, Y. (2018). Quasi-6-day wave effects on the equatorial ionization anomaly over a solar cycle. *Journal of Geophysical Research: Space Physics*, *123*, 9881–9892. https://doi.org/10.1029/2018JA026014

Yamazaki, Y., Matthias, V., Miyoshi, Y., Stolle, C., Siddiqui, T., Kervalishvili, G., et al. (2020). September 2019 Antarctic sudden stratospheric warming: Quasi-6-day wave burst and ionospheric effects. *Geophysical Research Letters*, *47*, e2019GL086577. https://doi.org/10.1029/2019GL086577

Yamazaki, Y., & Miyoshi, Y. (2020). *Simulation Data From GAIA (Ground-to-Topside Model of Atmosphere and Ionosphere for Aeronomy) for the September 2019 Sudden Stratospheric Warming Event*, GFZ, Potsdam, Germany: GFZ Data Services. http://doi.org/10.5880/GFZ.2.3.2020.004

Yamazaki, Y., Stolle, C., Matzka, J., & Alken, P. (2018). Quasi-6-day wave modulation of the equatorial electrojet. *Journal of Geophysical Research: Space Physics*, *123*, 4094–4109. https://doi.org/10.1029/2018JA025365